Giant angular-dependent Nernst effect in the quasi-one-dimensional organic conductor $(\text{TMTSF})_2\text{PF}_6$

Weida Wu,* N. P. Ong, and P. M. Chaikin

Department of Physics, Princeton University, Princeton, New Jersey 08544, USA

(Received 26 July 2005; published 22 December 2005)

We present a detailed study of the Nernst effect S_{zx} in $(\text{TMTSF})_2\text{PF}_6$ as a function of temperature, magnetic field magnitude, direction, and pressure. As previously reported there is a large resonantlike structure as the magnetic field is rotated through crystallographic directions, the Lebed magic angles. These Nernst effect resonances strongly suggest that the transport of the system is effectively "coherent" only in crystallographic planes along or close to the applied field direction. We also present analytical and numerical calculations of the conductivity and thermoelectric tensors for $(\text{TMTSF})_2\text{PF}_6$, based on a Boltzmann transport model within the semiclassical approximation. The Boltzmann transport calculation fails to describe the experimental data. We suggest that the answer may lie in the field induced decoupling of the strongly correlated chains.

I. INTRODUCTION

$(\text{TMTSF})_2\text{PF}_6$ is a quasi-one-dimensional (Q1D) electronic system, which displays various ground states ranging from triplet superconductor[1–3] to spin-density wave (SDW) insulator, depending on pressure, temperature, and magnetic field (for a review, please see Ref. 4). $(\text{TMTSF})_2\text{PF}_6$ consists of platelike TMTSF molecules which stack with a strong wave function overlap in chains. The intrachain bandwidth is ~1 eV while the interchain couplings give anisotropic bandwidths of 0.1 eV and 0.003 eV in the approximately orthogonal directions. In the "metallic" phase under moderate magnetic field, a fascinating phenomenon, the so-called Lebed magic angle effect (MAE) was discovered[5–7] after Lebed's initial prediction.[8,9] The manifestations of these MAEs were sharp resistance dips when the magnetic field was aligned at interchain directions in real space (lattice vectors[10]). In reciprocal space a field along the magic angles induces electron motion along commensurate **k** space orbits.[11] Despite many theoretical efforts to describe the magic angle effects,[10–17] there is as yet no satisfactory explanation. Most of the theories focus on the semiclassical motions of electrons on the open Fermi surface derived from the single particle band structure.

Recently, a giant Nernst effect was determined in $(\text{TMTSF})_2\text{PF}_6$ under pressure.[18] As the magnetic field was rotated toward a magic angle, the Nernst signal increased then decreased toward zero, changed sign at the magic angle, and continued in an inverse manner. The result is a sharp resonantlike structure. The magnitude of the Nernst signal at 1 K is at least three orders of magnitude larger than what we expected from simple (Drude) estimations. The sign change of the Nernst effect at the magic angles strongly suggests that the transport involved in the Nernst effect is effectively two-dimensional (2D) at these commensurate angles. Both the sign change at the magic angles and the large magnitude of the signal are not yet explained, but the effect appears generic for these materials. The giant resonant Nernst voltage has been observed in the sister compound $(\text{TMTSF})_2\text{ClO}_4$ (Ref. 19). Present phenomenological models for the sign

change involve field induced interplane decoupling.[10] Although there is some experimental evidence for this decoupling, there are not yet theoretical models which rigorously demonstrate this phenomenon.

Giant Nernst signals have also been seen in high transition temperature superconducting (HT$_c$) cuprates, where a model invoking superconducting vortices and 2D superconducting phase coherence has been successful.[20–22] A similar model has been proposed for $(\text{TMTSF})_2\text{PF}_6$.[17] However, to apply this idea in $(\text{TMTSF})_2\text{PF}_6$ is quite controversial. On one hand it naturally explains the large Nernst signal with undetectable thermopower signal, predicts a particular sign of the Nernst effect confirmed by experiments, and qualitatively explains some aspects of experiments. On the other hand, it predicts a large superconducting fluctuation region in the phase diagram, which is absent in other measurements. Most of the superconducting properties in $(\text{TMTSF})_2\text{PF}_6$ have been understood within a mean field BCS picture. We will explore the possibility of this vortex Nernst effect with more experimental detail in a subsequent paper.

What sorely hampers progress in understanding these unusual magic angle phenomena are the lack of measurements other than charge transport. The field induced SDW (FISDW) and MAE have been observed primarily in the charge channel by transport measurements. The FISDW has been more thoroughly explored with magnetization, magnetocaloric effect, and spin relaxation studies. Magnetic torque measurements on $(\text{TMTSF})_2\text{ClO}_4$ suggest there is a thermodynamic component to the MAE.[6] While a thermodynamic probe is an obvious choice for establishing the presence of unknown phases or fluctuations in $(\text{TMTSF})_2\text{PF}_6$, the high pressure environment makes a measurement of specific heat or dc magnetic susceptibility impractical. Recently, the ^{77}Se NMR spin-lattice relaxation rate measurements[23] at different magnetic field orientation show no evidence for either a spin gap or a single particle gap. Furthermore, there is no evidence for an enhancement of the FISDW transition temperature. This strongly suggests that neither FISDW ordering nor fluctuations are likely to be responsible for the MAE. The dramatic contrast between the charge channel and the spin
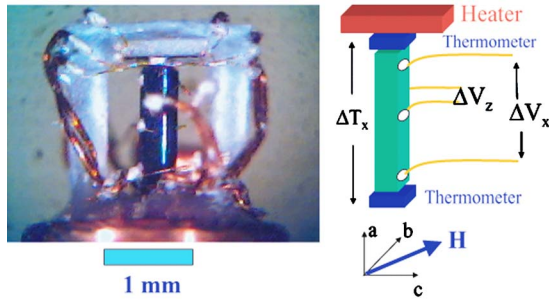
FIG. 1. (Color online) The measurement setup of the Nernst effect S_{zx}: Three pairs of Au wires were attached to the sample along the a axis on the opposite sides of the **ab** faces of the sample. Two RuO thin film resistance thermometers were placed next to both ends of the sample to measure the temperature gradient generated by a miniature heater on the top. The middle pair of leads was used for Nernst voltage ΔV_z pickup. The other two pairs of leads were used for four-probe interplane (c axis) resistance measurements. The magnetoresistance R_{zz}, was measured simultaneously with the Nernst effect S_{zx}.

FIG. 2. The angular dependence of the Nernst signal S_{zx} and c axis resistance R_{zz} were measured simultaneous at 1 K, 6 T, and 13 kbar. The thin line data are $R_{zz}(\theta)$. The open circles are the Nernst data $S_{zx}(\theta)$. The solid line is a guide to the eyes. The Nernst resonances are well aligned with the magic angles marked by the resistance dips. Here ±1 correspond to interchain directions $\mathbf{c}' \pm \mathbf{b}'$.

channel at magic angles suggests that spin and charge degrees of freedom may be decoupled.[24,25] The thermodynamic and suggested coherent-incoherent transitions would therefore be the result of interaction and correlation effects due to subtle changes in the electronic wave functions and density wave susceptibilities.

Before speculating further on exotic mechanisms for the giant Nernst resonances and other MAEs in transport it is necessary to see what conventional transport theory will yield. Although Boltzmann transport calculations as a function of magnetic field magnitude and direction have been performed for resistance[11] there has been no such study for the thermoelectric transport coefficients. Such calculations are one of the main contributions of this paper.

We divide our presentation into two sections. The first section focuses on the Nernst experiments. We present a detailed study of the Nernst effect S_{zx} in (TMTSF)$_2$PF$_6$ at various pressures, magnetic fields, and temperatures. The second part presents both numerical and analytic calculations of Boltzmann transport in the relaxation time approximation with realistic band parameters. We then compare the calculations with our experiment data.

II. NERNST MEASUREMENT

A. Method

Figure 1 shows the experimental setup for the Nernst effect S_{zx} measurement with the temperature gradient along the a axis and the electric field measured along c axis. Three pairs of Au wires were attached to the opposite **ab** faces of the sample by silver paint for both resistance measurements (the end pairs) and the Nernst measurements (the middle pair). The Au wires were attached to the alloy wires (phospher bronze) and fed through the pressure cell base. Here we used low thermal conductivity alloy wires instead of Cu wires to minimize the possible transverse temperature gradients. A miniature heater was placed on top of the sample to
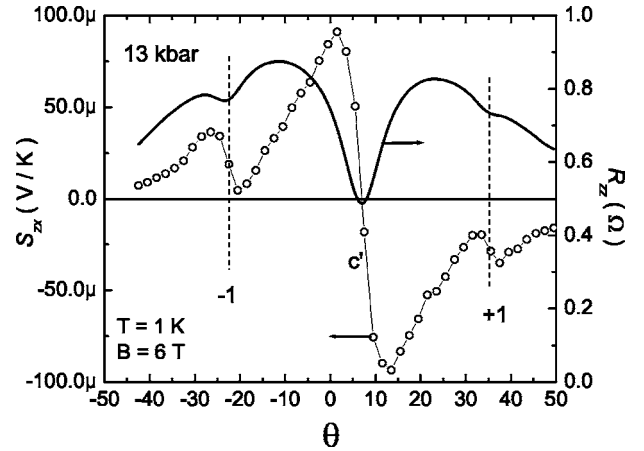
establish a small temperature gradient along the a axis. Two thin film RuO thermometers were used to measure the temperature difference. The thermoelectric voltage is measured by a Keithley 182 Nanovoltmeter. The heater was turned on and off for a few cycles for signal averaging.[26] A linear-fit-extrapolation method was used to accommodate the slow drift of the baseline signal.[27] The resistance was measured by a conventional four-probe low frequency lock-in technique. The magnetoresistance R_{zz} and Nernst signals S_{zx} were measured simultaneously.

Figure 2 shows a typical angular dependence of the Nernst signal S_{zx} in (TMTSF)$_2$PF$_6$, obtained at 1 K, 6 T, and 13 kbar. The magnetic field was rotated from −40° to 50° with respect to the c^* axis (see Ref. 18 for definitions of $\mathbf{c}^*$, $\mathbf{c}'$, etc.). The maximum Nernst signal is about 100 μV/K, found at approximately 3°–4° off $\mathbf{c}'$ ($\theta_{c'} = 7°$). The Nernst coefficient is of the order of 10 μV/K T. As far as we know, this value is much larger than the Nernst effect observed in any other metal at low temperature. The angular dependence of the Nernst signal agrees well with our previous thermoelectric measurement in a different geometry.[18] To study the temperature, field, and pressure dependence of the giant Nernst effect, we fixed the magnetic field orientation at 3° off a magic angle($\mathbf{c}'$ or $-1L$). First, let us discuss the sign of the Nernst effect in (TMTSF)$_2$PF$_6$. This is very important for the vortex Nernst model.

B. The sign of the Nernst effect

In the vortex liquid phase of type II superconductors vortices flow down the temperature gradient, $\mathbf{v} \| (-\nabla T)$ and generate an electric field $\mathbf{E} = \mathbf{B} \times \mathbf{v}$ transverse to the temperature gradient $-\nabla T$ according to the Josephson relation.[28,29] Therefore, the sign of the vortex Nernst effect is fixed by $\nabla T \times \mathbf{B}$. In general, the Nernst effect of an electronic system can have either sign depending on details of the band structure. To determine the sign of the Nernst signal, we noted the orien-
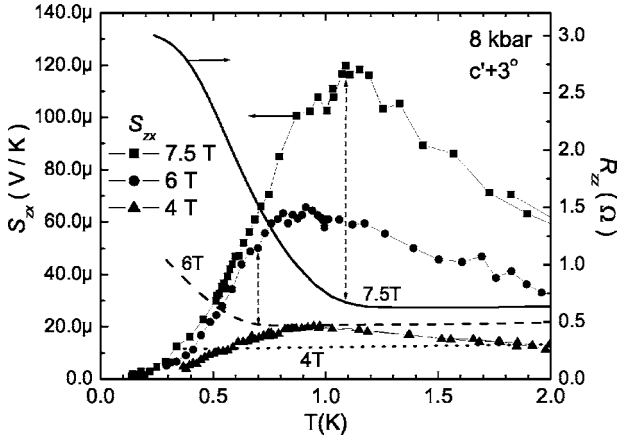
FIG. 3. Simultaneous measured temperature dependences of the c axis resistance R_{zz} (thin lines) and the Nernst signal S_{zx} (filled symbols) at 8 kbar for 3° off $\mathbf{c}'$. The Nernst signals rise to a maximum around 1 K, then fall exponentially and are unmeasurable below ~200 mK. The decrease of the Nernst signal is correlated with the upturn of the resistance as T decreases. The upturn of R_{zz} indicates the metal FISDW phase transition.
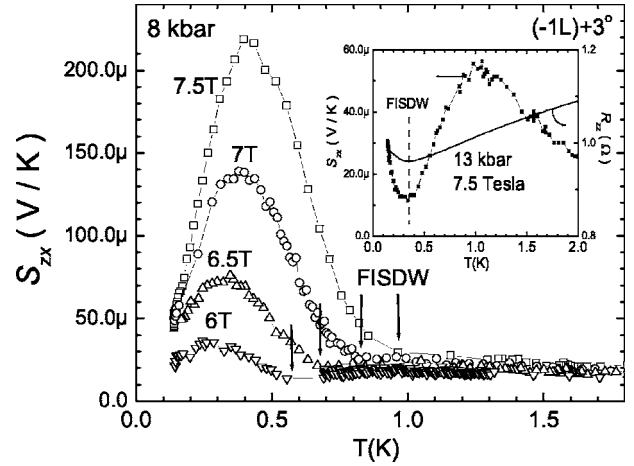

FIG. 4. Main panel: Temperature dependence of the Nernst signal S_{zx} measured at 3° away from −1 Lebed angle at 8 kbar. The magnetic fields are: 7.5, 7.0, 6.5, and 6.0 T, respectively. The arrows mark the FISDW transition temperature obtained from resistance measurements $R_{zz}(T)$ (not shown for clarity) at various fields. Inset: Temperature dependence of the Nernst signal S_{zx} and resistance R_{zz} of the −1 Lebed angle at 13 kbar for 7.5 T magnetic field. The dash line marks the FISDW transition (~350 mK). An enhancement of Nernst voltage was found in the FISDW phase.

tation of the sample and leads, and placed an alignment mark on the base (feedthrough) of the pressure cell and on the cell body. We assume the alignment mark does not change much on pressurization. To get the Nernst sign correct we need to know the orientation to better than 90°. We see the magic angles where we expect them to be within 15°. We observed no orientation variation when the pressure was increased in the same pressure cell. Our measurements show that the sign of the Nernst effect is consistent with the vortex Nernst model (but certainly does not prove it).

C. Temperature dependence

Figure 3 shows the temperature dependence of the Nernst effect S_{zx} at $\mathbf{c}'$ at different field values: 4, 6, and 7.5 T for 8 kbar pressure. The Nernst signals rise gradually to a maximum around 1 K as the temperature decreases, then fall off roughly exponentially at lower temperatures and are unmeasurable below ~200 mK. Clearly, the Nernst signal is nonlinear with the magnetic field below 2 K. The temperature dependence of the Nernst signal at 7.5 T agrees with the previous Nernst data from the thermopower measurement.[18] At high magnetic fields, (TMTSF)$_2$PF$_6$ enters the FISDW insulting phase at a critical temperature $T_c(H)$ indicated by the sharp rise of resistance R_{zz} measured simultaneously. In the "metallic" phase, the Nernst effect at $\mathbf{c}'$ and ±1 Lebed angles have similar temperature dependence, except the magnitude is much larger for $\mathbf{c}'$. However, the presence of the FISDW phase seems to suppress the Nernst signal at $\mathbf{c}'$. As shown in Fig. 3 for 7.5 T data, a sudden decrease of the Nernst voltage happens at the onset of the FISDW transition.

Interestingly, the presence of the FISDW phase affects the Nernst signal at the −1 Lebed angle differently. As shown in Fig. 4, at 8 kbar pressure the FISDW onsets (from R_{zz}) coincide with the onsets of a large increase of Nernst voltage at the −1 Lebed angle at various magnetic fields. At still lower

temperature the voltage at the −1 Lebed angle reaches a peak around 300~400 mK then decreases quickly. The peak value is as large as ~220 μV/K at 7.5 T. The difference is further confirmed by the angular dependence of the Nernst effect at base temperature (150 mK), where there are large Nernst resonances at the ±1 Lebed angles while there is none at $\mathbf{c}'$. This behavior is consistent with our previous measurements.[18] The effect of FISDW on −1 Lebed angles is further confirmed by measurements at higher pressures, where the FISDW transition temperatures $T_c(H)$ vary accordingly. For example, at 13 kbar the FISDW transition temperature at 7.5 T is suppressed down to ~350 mK, the enhancement of the Nernst effect at the −1 Lebed angle follows the FISDW transition accordingly as shown in the inset of Fig. 4.

The suppression of the Nernst signal at $\mathbf{c}'$ by the FISDW is not understood at this moment. It is probably due to the competition between the FISDW phase and metallic phase. This difference seems to suggest the magic angle $\mathbf{c}'$ is different from the −1 Lebed magic angle in a subtle way. In this paper, we limit our discussion within the "metallic" state where the MAE is pronounced. We note that a full understanding of the MAE should cover the FISDW phase, where the MAE is more complicated than in the metallic phase.

D. Field dependence

As seen in the temperature dependence of S_{zx} at different magnetic fields, the Nernst effect in (TMTSF)$_2$PF$_6$ is very nonlinear with the magnetic field. In the upper panel of Fig. 5, we show the simultaneous measurements of the magnetoresistance R_{zz} and the Nernst effect S_{zx} vs the magnetic field at 1.6 K, 8 kbar, and 3° off $\mathbf{c}'$. It is clear that the Nernst
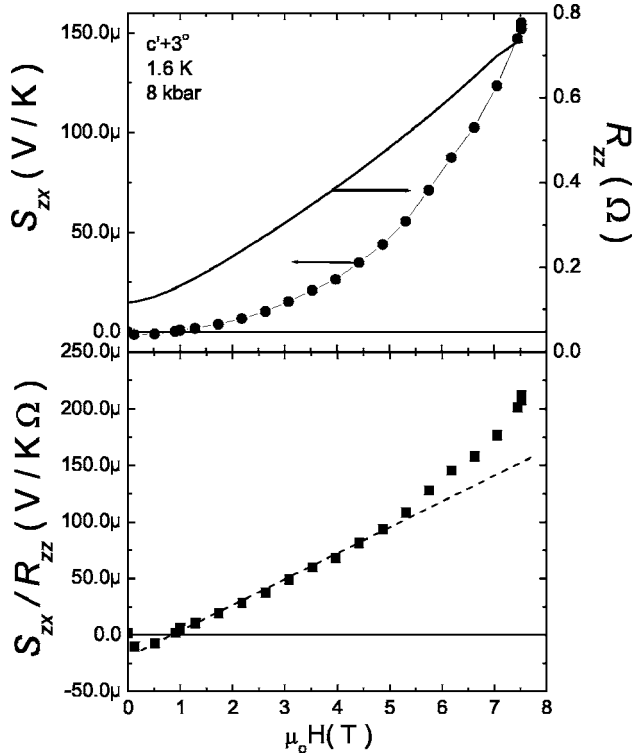
FIG. 5. Upper panel: Magnetic field dependence of S_{zx} and R_{zz} measured simultaneously at 8 kbar, 1.6 K for **c′**. Clearly S_{zx} is nonlinear with the magnetic field just as observed in the previous measurement (Ref. 18). Lower panel: Ratio of S_{zx} and R_{zz} derived from the upper panel. As discussed in the text, $S_{zx}/R_{zz} \propto \alpha_{zx}$. The dash line is a guide to the eyes. It is clear that at low field α_{zx} is linear with the field.

signal has a superlinear field dependence. An obvious nonlinear effect is the large magnetoresistance of $(TMTSF)_2PF_6$. In transport theory, the thermopower tensor $\overleftrightarrow{S}$ is the product of the resistivity tensor $\overleftrightarrow{\rho}$ and the thermoelectric tensor $\overleftrightarrow{\alpha}$

$$\overleftrightarrow{S} = \overleftrightarrow{\rho} \cdot \overleftrightarrow{\alpha}. \tag{1}$$

Therefore, $S_{zx} = \rho_{zx}\alpha_{xx} + \rho_{zy}\alpha_{yx} + \rho_{zz}\alpha_{zx} \approx \rho_{zz}\alpha_{zx}$. Here we ignore the first two terms since the Hall effects are negligibly small in the metallic phase for $(TMTSF)_2PF_6$. To obtain α_{zx}, we took the ratio of the Nernst signal S_{zx} and the resistance R_{zz} at the same field to obtain the field dependence of $\alpha_{zx} \propto (S_{zx}/R_{zz})$ according to Eq. (1). The prefactor depends on the sample geometry. The result is shown in the lower panel of Fig. 5. Clearly α_{zx} is approximately linear with the magnetic field below 5 T. Therefore, the nonlinearity of the Nernst signal S_{zx} in $(TMTSF)_2PF_6$ mainly comes from the large magnetoresistance. The linear field dependence for field along **c′** and −1 Lebed angle suggests that α_{zx} is probably a more fundamental quantity in the thermoelectric effect of $(TMTSF)_2PF_6$.

Figure 6 shows the field dependence of S_{zx} and R_{zz} for the field along 3° off the −1 Lebed angle at 375 mK. We can see that when the $(TMTSF)_2PF_6$ goes into the FISDW, the resistance rises up sharply around 5.5 T due to the presence of
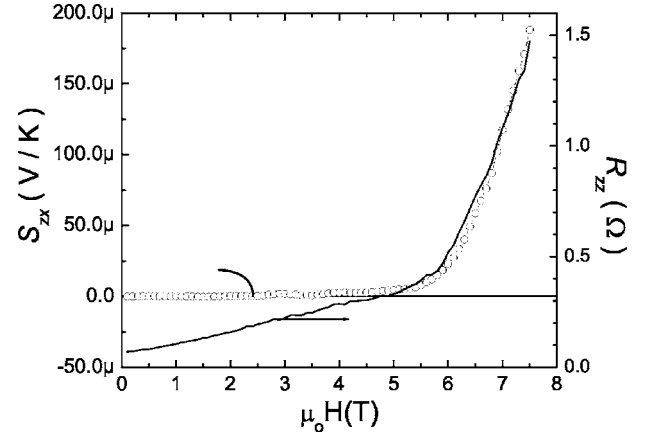

FIG. 6. Magnetic field dependence of S_{zx} and R_{zz} measured simultaneously at 8 kbar and 375 mK for the field at 3° away from −1 Lebed angle. The upturn of the R_{zz} around 5.5 T defines the threshold field of the FISDW transition. S_{zx} is highly nonlinear and enhanced greatly in the FISDW phase.

the FISDW gap. The Nernst signal also shows a sharp upturn around 5.5 T and rises up dramatically. This agrees with the observation of the enhancement of the Nernst signal at a −1 Lebed angle in the temperature dependence (Fig. 4).

E. The effect of pressure

The ground state properties of the Bechgaard salts are strongly affected by hydrostatic pressure. The temperature, pressure, and magnetic field (T-P-H) three dimensional (3D) phase diagram (Fig. 1 in Ref. 30) summarizes the effects of pressure on various phase transitions. For example, the threshold field of the FISDW phase progressively increases as the pressure gets higher. The superconducting transition temperature T_c is also slowly suppressed by increasing pressure. Figure 7 shows the zero field temperature dependence of resistance R_{zz} at 8 kbar, 10 kbar, and 13 kbar, respectively. The superconducting transition temperature decreases
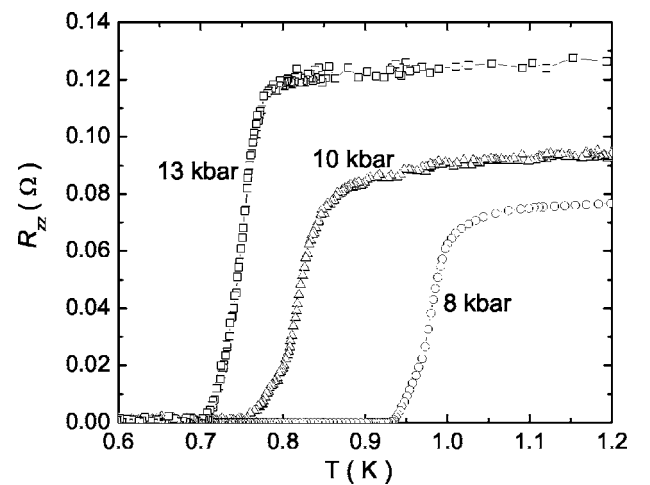

FIG. 7. Zero field temperature dependence of R_{zz} at 8, 10, and 13 kbar. The T_{c0}'s are 1.02 K, 0.87 K, and 0.77 K, obtained from the $R_{zz}(T)$, respectively.
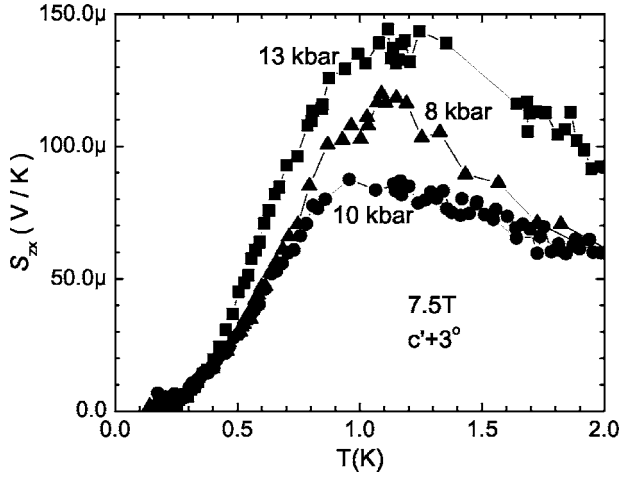
FIG. 8. Temperature dependence of the Nernst signal S_{zx} at 8, 10, and 13 kbar at 7.5 T. Qualitatively no change is observed for various pressures.

slowly with increasing pressure. Using the onset definition (90% of the normal state value), we found that the superconducting transition temperatures T_{c0} are 1.02 K, 0.87 K, and 0.77 K, respectively.

In Fig. 8 we show the comparison of the temperature dependence of the normalized Nernst signal at 3° off **c′** between 8 kbar, 10 kbar, and 13 kbar. Qualitatively, the temperature dependence of the Nernst signal is pressure insensitive.

The angular dependence doesn't change significantly either as we vary the pressure. Figure 9 shows the angular dependence of S_{zx} and R_{zz} at 8, 10, and 13 kbar, respectively. Note that the temperature and magnetic fields of these data are not identical. However, qualitatively they are all the same. Note that all data shown here are in the metallic phase.

III. BOLTZMANN CALCULATION OF THE NERNST EFFECT

To gain some elementary intuition about transport processes it is often instructive to look first at a generalized Drude approximation, by which we mean a classical gas of charged particles in the lowest order response to an applied set of driving fields.

A. Drude transport

In Fig. 10 we show a cartoon of the particle motion of such a charged gas. In a Drude model forces accelerate particles which then lose momentum in collisions at a rate $1/\tau$. The basic equation of motion is therefore $m\mathbf{v}/\tau=\mathbf{F}$, the charge per particle is q, the particle density is n, the current density is simply charge density times velocity $\mathbf{j}=nq\mathbf{v}$ and $\mathbf{j}=\sigma\cdot\mathbf{E}$. In Fig. 10(a), $\mathbf{F}$ is $q\mathbf{E}$ and $\mathbf{v}=(q\tau/m)\mathbf{E}$, $\mathbf{j}=(nq^2\tau/m)\cdot\mathbf{E}$, the conductivity σ is given by $\sigma=nq^2\tau/m$. In the presence of the magnetic field there is a Lorentz force which deflects particles in the y direction building up charges on the upper and lower boundaries. The charges continue accumulating until the electric field they generate exactly
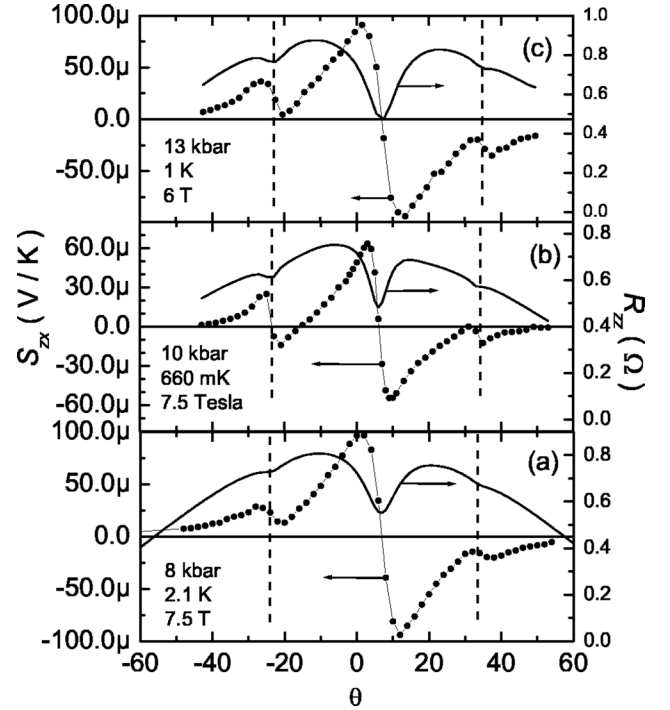

FIG. 9. (Color online) Angle dependence of S_{zx} ("●") and R_{zz} (lines) at (a) 8 kbar, 2.1 K, and 7.5 T; (b) 10 kbar, 660 mK, and 7.5 T; (c) 13 kbar, 1 K, and 6 T. Qualitatively, no change is observed.

cancels the Lorentz force, $E_y=v_x B_z$. In the steady state the Hall field $E_y=j_x/nq\cdot B_z$ completely compensates the effect of the magnetic field, the carriers only drift in the x direction and there is no magnetoresistance. In Fig. 10(b) the drive is a temperature gradient. In this simple model the gas is ideal and we use the ideal gas law, $P=nk_BT$. A temperature gradient translates to a pressure gradient $\nabla P=nk_B\nabla T$, or a force per particle of $\mathbf{F}=\nabla P/n$. The charged particles will flow in the x direction charging the boundaries and creating an opposing field E_x. The current and charging stop when $qE_x=F_x$ or $E_x=(k_B/q)\nabla_xT$. This thermoelectric voltage is the Seebeck effect with coefficient $S_1=k_B/q$. This was a big failure of the Drude model. It overestimates the thermopower by several orders of magnitude. The reason is quite evident today. We have a degenerate electron gas (DEG) rather than an ideal classical gas. The effective number of degrees of freedom, or particles that can transport heat, is reduced by $\sim k_BT/E_F$ so the $S_{1DEG}\sim(k_BT/E_F)(k_B/q)$. In this picture the electric force cancels the pressure and the particles have no velocity, $\mathbf{v}\times\mathbf{B}=0$ and the Nernst voltage is zero. For the simplest conductors we therefore expect the thermopower to be sizeable and the Nernst effect negligible. But it is worth noting that effectively the same argument would suggest that the magnetoresistance is negligible.

In Figs. 10(c) and 10(d) we consider the case of two oppositely charged carriers, which are otherwise identical. With an electric field along x the two carriers move at $v_x=(q\tau/m)E_x$ in opposite directions both contributing to the electrical current and conductivity which remains $\sigma_0=nq^2\tau/m$. Now however, in the presence of B_z both are deflected in the same direction, there is no charge accumulated
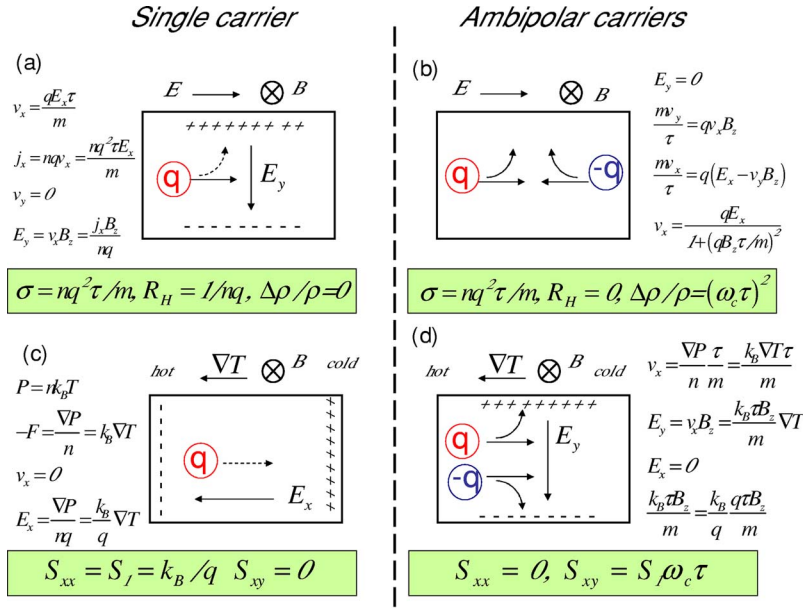
FIG. 10. (Color online) Generalized Drude model schematic. Magnetic field perpendicular to the plane. (a) and (b) show the electric field **E** drive, (c) and (d) show temperature gradient ∇T drive, (a) and (c) show a single type of charge carrier, and (b) and (d) show two oppositely charged carriers (ambipolar).

on the boundaries, there is no Hall voltage, and velocities persist in both directions, $v_y = v_x(qB_z\tau/m)$, $v_x = (q\tau/m)E_x - v_y(qB_z/m)\tau$, with the solution, $v_x = (q\tau m)E_x/[1+(qB_z\tau/m)^2]$, $\sigma = \sigma_0/[1+(\omega_c\tau)^2]$, where $\omega_c = |q|B_z/m$. There is now magnetoresistance, $\Delta\rho/\rho = (\omega_c\tau)^2$. In Fig. 10(d) the drive is a temperature gradient again producing a pressure gradient. Both types of particles move down the pressure gradient with velocity, $v_x = k_B\nabla_xT\tau/m$ there is no charge accumulation, and no field generated along x so the Seebeck coefficient is zero. In the presence of a magnetic field, the particles with the same velocity but opposite sign are separated, charges accumulate on the upper and lower boundaries until the electric field compensates the Lorentz force, $E_y = v_xB_z = k_B\nabla_xT\tau B_z/m$. The result is a Nernst voltage with coefficient $S_{yx} = k_B\tau B_z/m = (k_B/|q|)(|q|B_z\tau/m) = S_1\omega_c\tau$. With the degenerate electron gas correction we should then expect $S_{xyDEG} \sim (k_B/|q|)(k_BT/E_F)(\omega_c\tau)$,

	σ	Hall	MR	Seebeck	Nernst
One carrier	$\dfrac{nq^2\tau}{m}$	$\dfrac{1}{nq}$	0	$\dfrac{k_B}{q}\dfrac{k_BT}{E_F}$	0
Ambipolar	$\dfrac{nq^2\tau}{m}$	0	$(\omega_c\tau)^2$	0	$\dfrac{k_B}{|q|}\dfrac{k_BT}{E_F}\omega_c\tau$

The extension of these results to field orientation and different ratios of the densities of the oppositely charged particles is straightforward. With

$$S_1 = \frac{k_B}{|q|}\frac{k_BT}{E_F}, \qquad a = \frac{n^+ - n^-}{n^+ + n^-},$$

$$f(a) = a\frac{1+(\omega_c\tau)^2}{1+a^2(\omega_c\tau)^2}, \qquad g(a) = \frac{1-a^2}{1+a^2(\omega_c\tau)^2},$$

we find $S(a) = S_1f(a)$, $S_{xy}(a) = S_1(\omega_c\tau)g(a)$, $R_H = 1/n|q|f(a)$, $\Delta\rho/\rho = (\omega_c\tau)^2g(a)$. The Hall and Nernst voltages vary as $\mathbf{B}\times\mathbf{E}$ and $\mathbf{B}\times\nabla T$, respectively. $f(a)$ and $g(a)$ are plotted in Fig. 11. Putting in realistic parameters, one will find that the Nernst effect in the Drude model is of the order of 10 nV/K. The Drude picture also predicts that the Nernst effect has a simple $\sin\theta$ dependence of magnetic field orientation and linear dependence of magnetic field strength B and temperature T.

B. Boltzmann transport and Q1D Fermi surface

Simple Drude calculations are not capable of handling the highly anisotropic nature of the Bechgaard salts nor the
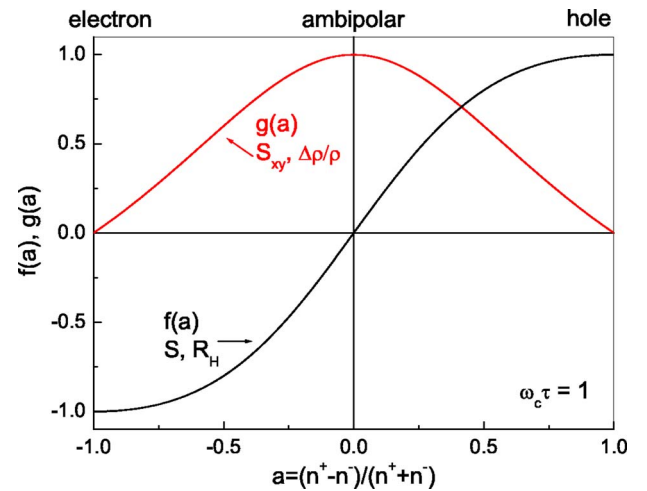

FIG. 11. (Color online) The Drude picture in general: Here $a = (n^+ - n^-)/(n^+ + n^-)$ is the net charge density of mobile charge carriers. The thermopower S and the Hall effect R_H scale with $f(a)$, while the Nernst effect S_{xy} and the magnetoresistance $\Delta\rho/\rho$ scale with $g(a)$.

angular orientation of the field relative to the lattice vectors. The simplest treatment which includes the bandstructure comes from a steady state Boltzmann equation. It has previously been shown that Boltzmann transport, appropriately modified to follow electron trajectories over many Brillouin zones (or equivalently many Umklapp scatterings) can give a magic angle effect in R_{zz}.[11,12] Moreover, this model is in qualitative agreement with the measurements in the (TMTSF)$_2$ClO$_4$ salt. Although the Boltzmann transport [the Osada model for (TMTSF)$_2$X] have not been successful for (TMTSF)$_2$PF$_6$, they are still the only reasonable single particle treatment available. We therefore performed both numerical and analytic calculations using a Boltzmann Transport formulation based on the tight binding approximation band structure within the single relaxation time approximation. For simplicity, the triclinic crystal structure of (TMTSF)$_2$X is taken as orthorhombic.

$$\varepsilon = -2t_a \cos k_x a - 2t_b \cos k_y b - 2t_c \cos k_z c. \quad (2)$$

For (TMTSF)$_2$X, $t_a \gg t_b \gg t_c$. Often people linearize the k_x dispersion for simplicity. One would obtain the so-called linearized dispersion

$$\varepsilon - \varepsilon_f = \pm \hbar v_f (k_x \mp k_f) - 2t_b \cos(k_y b) - 2t_c \cos(k_z c). \quad (3)$$

In this approximation, the Fermi velocity v_f [or the density of states on Fermi surface $N_f(\varepsilon_f) = 1/\hbar v_f$] is a constant for a given energy. Many of the angular magnetoresistance oscillations (AMRO), e.g., the Danner-Kang-Chaikin oscillation (**ac** rotation),[31] the third angle effect (**ab** rotation),[32] and the combination of them[33] can be understood within this approximation. There is excellent agreement between experiment and theory, especially for (TMTSF)$_2$ClO$_4$.[34] However, for a linearized dispersion relation the Hall effect is zero ($\sigma_{xy} = \sigma_{xz} = 0$). It is not surprising the Nernst effect is also zero ($S_{xy} = S_{xz} = 0$) in this approximation. In order to calculate the Nernst effect, we have to use the full dispersion or a nonlinear approximation in either numerical computation or in an analytic calculation.

In general transport theory, we consider both an electric current **J** and a thermal current $\mathbf{J}_q$ in response to an electric field **E**, a magnetic field **B**, and a temperature gradient ($-\nabla T$)

$$\mathbf{J} = \overleftrightarrow{\sigma} \cdot \mathbf{E} + \overleftrightarrow{\alpha} \cdot (-\nabla T),$$

$$\mathbf{J}_q = T \overleftrightarrow{\alpha}' \cdot \mathbf{E} + \overleftrightarrow{\kappa} \cdot (-\nabla T). \quad (4)$$

Here $\overleftrightarrow{\sigma}$ is the electric conductivity tensor, $\overleftrightarrow{\alpha}$ and $\overleftrightarrow{\alpha}'$ are the thermoelectric tensors, and $\overleftrightarrow{\kappa}$ is the thermal conductivity tensor. Here $\alpha_{ij}(\mathbf{H}) = \alpha'_{ji}(-\mathbf{H})$ according to the Onsager relation.[35,36] For a degenerate electron gas, these coefficients can be obtained by applying the relaxation time approximation[37]

$$\overleftrightarrow{\sigma} = \frac{e^2 \tau}{4\pi^3} \int_{\varepsilon=\mu} \frac{dS_k}{\hbar v} \mathbf{v} \langle \mathbf{v} \rangle,$$

$$\overleftrightarrow{\alpha} = \frac{1}{eT} \frac{\pi^2}{3} (k_B T)^2 \frac{\partial \overleftrightarrow{\sigma}(\varepsilon)}{\partial \varepsilon} \bigg|_{\varepsilon=\mu}. \quad (5)$$

Here we assume an energy and momentum independent relaxation time τ. The velocity average is defined as $\langle \mathbf{v}[\mathbf{k}(t)] \rangle \equiv \int_{-\infty}^{0} dt/\tau e^{t/\tau} \mathbf{v}[\mathbf{k}(t)]$, where $\mathbf{k}(t)$ is the semiclassical motion of electrons on a Fermi surface in the presence of a magnetic field. Equation (5) are the starting point of our calculation. From the general transport equations [Eq. (4)], by setting **J**=0 as the boundary condition in thermoelectric measurements, one would find Eq. (1). The Nernst signal S_{zx} is an off-diagonal element of the thermoelectric power tensor $\overleftrightarrow{S}$.

Now let's focus on the Q1D system (TMTSF)$_2$X. The Fermi surface of Q1D system consists of two slightly warped sheets. In order to evaluate the Fermi surface averaging velocity $\langle \mathbf{v} \rangle$ we have to calculate the motion of electrons on a Fermi surface in the presence of the magnetic field. Here the a axis (k_x) is the best conductivity direction, so the Fermi surface is approximately normal to the k_x axis. Therefore, k_x is a function of k_y, k_z, and ε from the dispersion relation [Eq. (2)], i.e.,

$$k_x = k_x(k_y, k_z; \varepsilon). \quad (6)$$

Therefore, k_x is not an independent variable for the semiclassical motion of electrons, given that the motion of the election is confined to the Fermi surface in the presence of the magnetic field **B**. The equations of motion can be reduced to

$$\frac{dk_y}{dt} = \frac{e}{\hbar}(v_z B_x - v_x B_z), \quad \frac{dk_z}{dt} = \frac{e}{\hbar}(v_x B_y - v_y B_x). \quad (7)$$

By solving these two equations of motion Eq. (7), we can evaluate $\mathbf{v}(t) = \mathbf{v}[\mathbf{k}(t)]$. This is what we need for the conductivity tensor $\overleftrightarrow{\sigma}$. From Eqs. (5), the thermoelectric coefficient tensor $\overleftrightarrow{\alpha}$ is proportional to the energy derivative of the conductivity tensor $\overleftrightarrow{\sigma}(\varepsilon)$ at the Fermi energy,

$$\sigma_{ij} = \frac{e^2 \tau}{4\pi^3} \int \int \frac{dk_y dk_z}{\hbar |v_x|} v_i \langle v_j \rangle,$$

$$\alpha_{ij} = \frac{k_B^2 e \tau T}{12\pi} \frac{\partial}{\partial \varepsilon} \int \int \frac{dk_y dk_z}{\hbar |v_x|} v_i \langle v_j \rangle. \quad (8)$$

In our analytic calculation, we derived an approximate analytic form for $\overleftrightarrow{\sigma}(\varepsilon)$, then obtained α by differentiation. On the other hand, it is straightforward to evaluate both $\overleftrightarrow{\sigma}$ and $\overleftrightarrow{\alpha}$ via numerical methods. Numerically $\overleftrightarrow{\alpha}$ can be calculated by taking the energy derivative of each term in the integral [Eq. (8)].
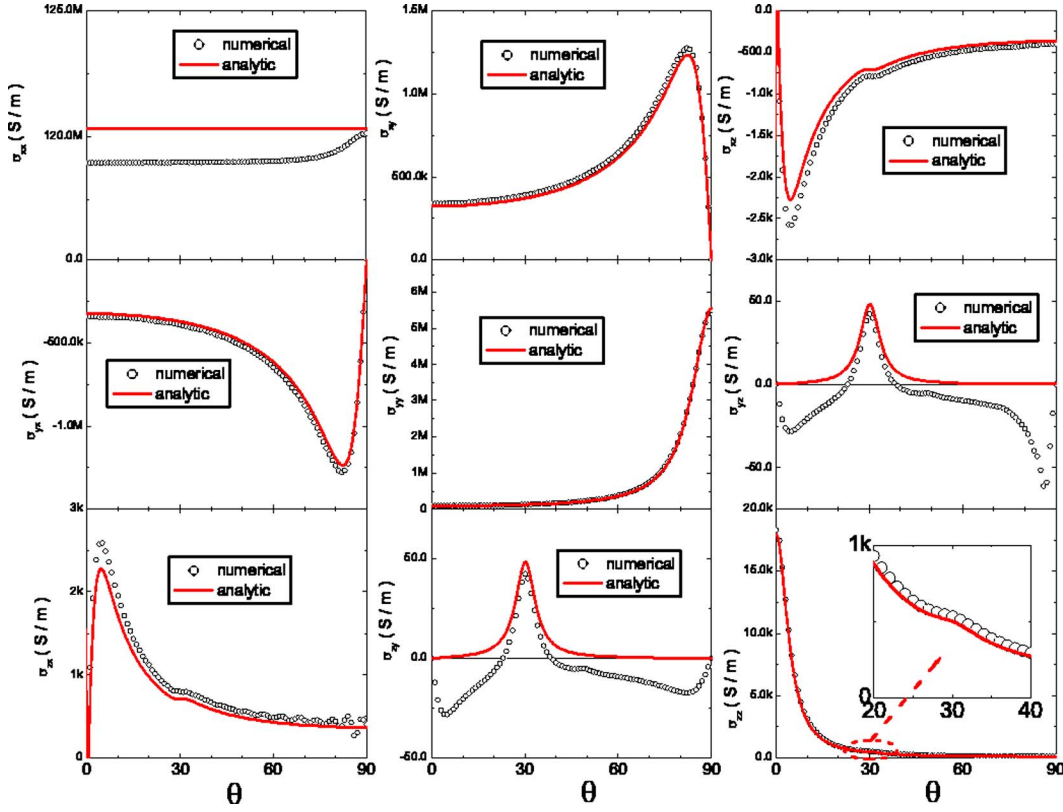
FIG. 12. (Color online) Angular dependence of conductivity tensor $\overset{\leftrightarrow}{\sigma}$. Here **B**=8 T. The origin is the c axis, while 90° is the b axis and 30° is the +1 Lebed angle: $c+b$. The inset of σ_{zz} shows a hump at the +1 Lebed angle. The open circles are the numerical calculations, and the thin lines are the analytic results.

C. Numerical calculation

From Eq. (8) we can obtain

$$\overset{\leftrightarrow}{\alpha} = \frac{k_B^2 e \tau T}{12\pi\hbar} \int\int dk_y dk_z \left[\underbrace{\frac{\partial}{\partial\varepsilon}\left(\frac{1}{|v_x|}\right) \mathbf{v}\langle\mathbf{v}\rangle}_{(a)} + \underbrace{\frac{1}{|v_x|}\frac{\partial\mathbf{v}}{\partial\varepsilon}\langle\mathbf{v}\rangle}_{(b)} \right.$$

$$\left. + \underbrace{\frac{1}{|v_x|}\mathbf{v}\frac{\partial\langle\mathbf{v}\rangle}{\partial\varepsilon}}_{(c)} \right]. \qquad (9)$$

Note here $\overset{\leftrightarrow}{\alpha} \propto T$ if we assume τ is T independence, which is a good approximation at low temperature. It is straightforward to evaluate the first two terms. Here we have

$$\frac{\partial\mathbf{v}}{\partial\varepsilon} = \hbar \cdot \overset{\leftrightarrow}{M}^{-1} \cdot \frac{\partial\mathbf{k}}{\partial\varepsilon}. \qquad (10)$$

Here we define the inverse mass tensor $\overset{\leftrightarrow}{M}^{-1}$ as

$$(\mathcal{M}^{-1})_{ij} = \frac{1}{\hbar}\frac{\partial v_i}{\partial k_j} = \frac{1}{\hbar^2}\frac{\partial^2\varepsilon(\mathbf{k})}{\partial k_i \partial k_j}. \qquad (11)$$

Here k_y and k_z are independent variables, so the energy dependence of the first two terms only comes from k_x, which is a function of ε [see Eq. (6)]. Then, we will have

$$\frac{\partial}{\partial\varepsilon} = \frac{\partial k_x}{\partial\varepsilon}\frac{\partial}{\partial k_x} = \frac{1}{\hbar v_x}\frac{\partial}{\partial k_x}. \qquad (12)$$

Therefore $(\partial/\partial\varepsilon)(1/v_x) = -(m_{xx}^{-1}/v_x^3)$ and $\partial v_i/\partial\varepsilon = \delta_{i,x}(m_{xx}^{-1}/v_x)$. For the (c) term in Eq. (9), we exchange the differentiation and averaging (integral), i.e., $(\partial\langle\mathbf{v}\rangle/\partial\varepsilon) = \langle\partial\mathbf{v}/\partial\varepsilon\rangle$. Setting the (a), (b), and (c) terms in Eq. (9) together, we obtain an expression for the thermoelectric coefficient tensor $\overset{\leftrightarrow}{\alpha}$,

$$\overset{\leftrightarrow}{\alpha} = \overset{\leftrightarrow}{\alpha}^{(+)} + \overset{\leftrightarrow}{\alpha}^{(-)}, \qquad (13)$$

where $\overset{\leftrightarrow}{\alpha}^{(\pm)}$ is defined as

$$\alpha_{ij}^{(\pm)} \equiv \frac{k_B^2 e \tau T}{12\pi\hbar} \int\int dk_y dk_z (\pm) \left[-\frac{m_{xx}^{-1}}{v_x^3}v_i\langle v_j\rangle + \frac{m_{xx}^{-1}}{v_x^2}\delta_{i,x}\langle v_j\rangle \right.$$

$$\left. + \frac{v_i}{v_x}\left\langle\frac{\partial v_j}{\partial\varepsilon}\right\rangle \right], \quad k_x \gtrless 0. \qquad (14)$$

Now we need to find $(\partial\mathbf{v}/\partial\varepsilon)(t)$, which involves the motion of an electron in the magnetic field. $(\partial\mathbf{v}/\partial\varepsilon)(t)$ depends on the value of the Fermi energy not only through k_x, but also through k_y and k_z, because k_y and k_z are also functions of t when the electron is moving on the Fermi surface in the magnetic field. These functions depend on energy ε and the "initial" condition (k_y^0, k_z^0), i.e.,

$$k_y(t) = k_y(t; \varepsilon, k_y^0, k_z^0), \quad k_z(t) = k_z(t; \varepsilon, k_y^0, k_z^0). \qquad (15)$$
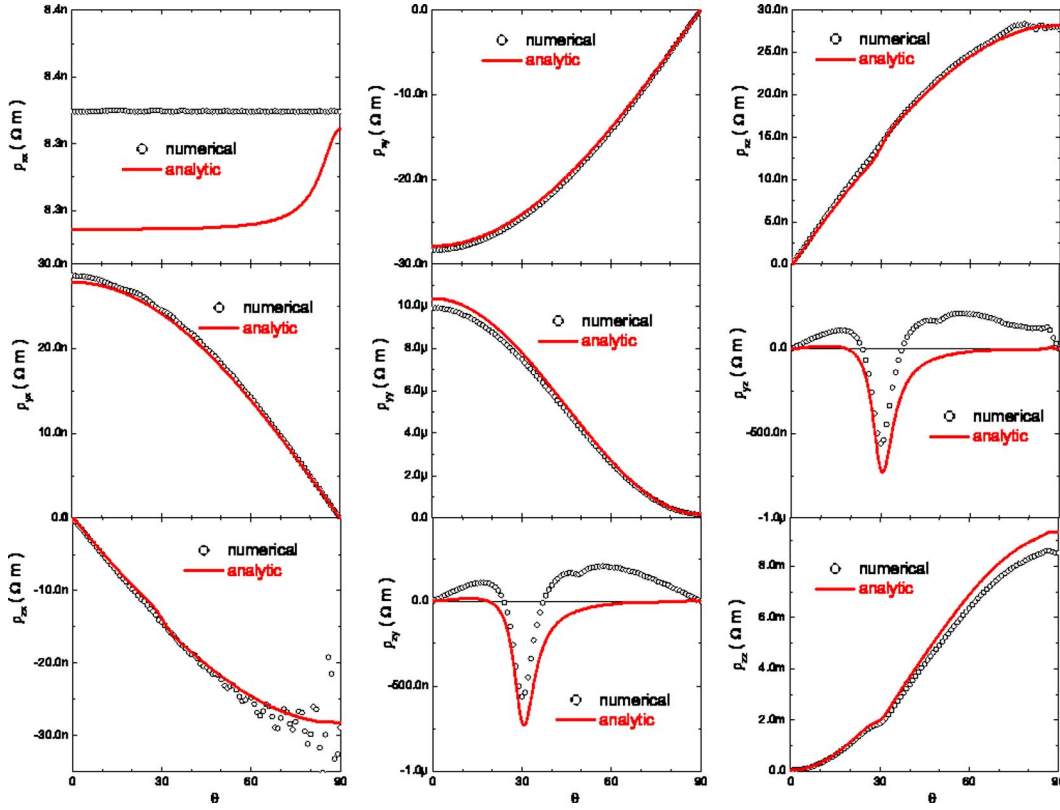
FIG. 13. (Color online) Resistivity tensor $\overleftrightarrow{\rho}=\overleftrightarrow{\sigma}^{-1}$.

We cannot derive the energy dependence of k_y and k_z directly if we don't know the solution of the equations of motion. However, we can find the differential equations which are satisfied by $\partial k_y/\partial\varepsilon$ and $\partial k_y/\partial\varepsilon$, from the equations of motion of k_y and k_z Eq. (7),

$$\frac{d}{dt}\frac{\partial k_y}{\partial\varepsilon} = \frac{\partial}{\partial\varepsilon}\frac{dk_y}{dt} = \frac{e}{\hbar}\left(\frac{\partial v_z}{\partial\varepsilon}B_x - \frac{\partial v_x}{\partial\varepsilon}B_z\right),$$

$$\frac{d}{dt}\frac{\partial k_y}{\partial\varepsilon} = \frac{\partial}{\partial\varepsilon}\frac{dk_z}{dt} = \frac{e}{\hbar}\left(\frac{\partial v_x}{\partial\varepsilon}B_y - \frac{\partial v_y}{\partial\varepsilon}B_x\right). \quad (16)$$

From Eq. (6), we will find

$$\frac{\partial k_x(t)}{\partial\varepsilon} = \frac{1}{\hbar v_x(t)}\left[1 - \hbar v_y(t)\frac{\partial k_y(t)}{\partial\varepsilon} - \hbar v_z(t)\frac{\partial k_z(t)}{\partial\varepsilon}\right]. \quad (17)$$

Combining Eq. (16) with Eq. (10), we can obtain numerical solutions of $(\partial\mathbf{v}/\partial\varepsilon)(t)$. Since k_y, k_z are independent of ε at $t=0$, the initial conditions for $(\partial k_y/\partial\varepsilon)(t)$ and $(\partial k_z/\partial\varepsilon)(t)$ are $(\partial k_y/\partial\varepsilon)(0)=(\partial k_z/\partial\varepsilon)(0)=0$.

In summary, to calculate both $\overleftrightarrow{\sigma}$ and $\overleftrightarrow{\alpha}$, we numerically solve two sets of equations of motions, Eqs. (7) and Eqs. (16). To treat the differential equations in Eqs. (7) and (16), we use a fourth order Runge-Kutta method.[38] Then we numerically integrate $\langle\mathbf{v}\rangle$ and $\langle\partial\mathbf{v}/\partial\varepsilon\rangle$ and evaluate both $\overleftrightarrow{\sigma}$ and $\overleftrightarrow{\alpha}$ by Fermi surface integrals. Here we use the band parameters (t_a=0.25 eV, t_b=0.024 eV, and t_c=0.008 eV) from tight binding approximations, realistic lattice parameters (a=3.49 Å, b=7.7 Å, and c=13.264 Å) and a scattering time

τ=4.26×10^{-12} sec from previous studies by Danner *et al.*[31] Here we use B=8 T, and T=1 K, which are comparable with experiment conditions. The combination of the parameters produce $\omega_c\tau=eB\tau/m_e$=6 for an isotropic free electron gas. We use a 20×20 grid on the Fermi surface in the calculations. Although the grid is a little rough, the results catch all the main features. We also used a 40×40 grid for some calculations and did not find a significant difference.

D. Analytic calculation

The basis of our analytic approximation scheme is finding the proper correction to the linear dispersion approximation Eq. (3). We expanded v_x to next order to include the effect of nonlinearity of the dispersion, i.e., $v_x\approx v_f+\delta v_f$. This approach is basically the semiclassical version of Lebed's quantum approach.[39] It is straightforward to find $v_f=(2t_a a/\hbar)\sin k_f a_0$ with $\cos k_f a=-\epsilon/2t_a$, and the first order correction is

$$\frac{\delta v_f}{v_f} = \frac{\cos k_f a}{\sin^2 k_f a}\left[\frac{t_b}{t_a}\cos(k_y b) + \frac{t_c}{t_a}\cos(k_z c)\right] + \cdots. \quad (18)$$

Defining $\beta\equiv(\cos k_f a/\sin^2 k_f a)(t_b/t_a)$ and $\gamma\equiv(\cos k_f a/\sin^2 k_f a)(t_c/t_a)$, then we have

$$v_x \approx v_f[1 - \beta\cos(k_y b) - \gamma\cos(k_z c)],$$

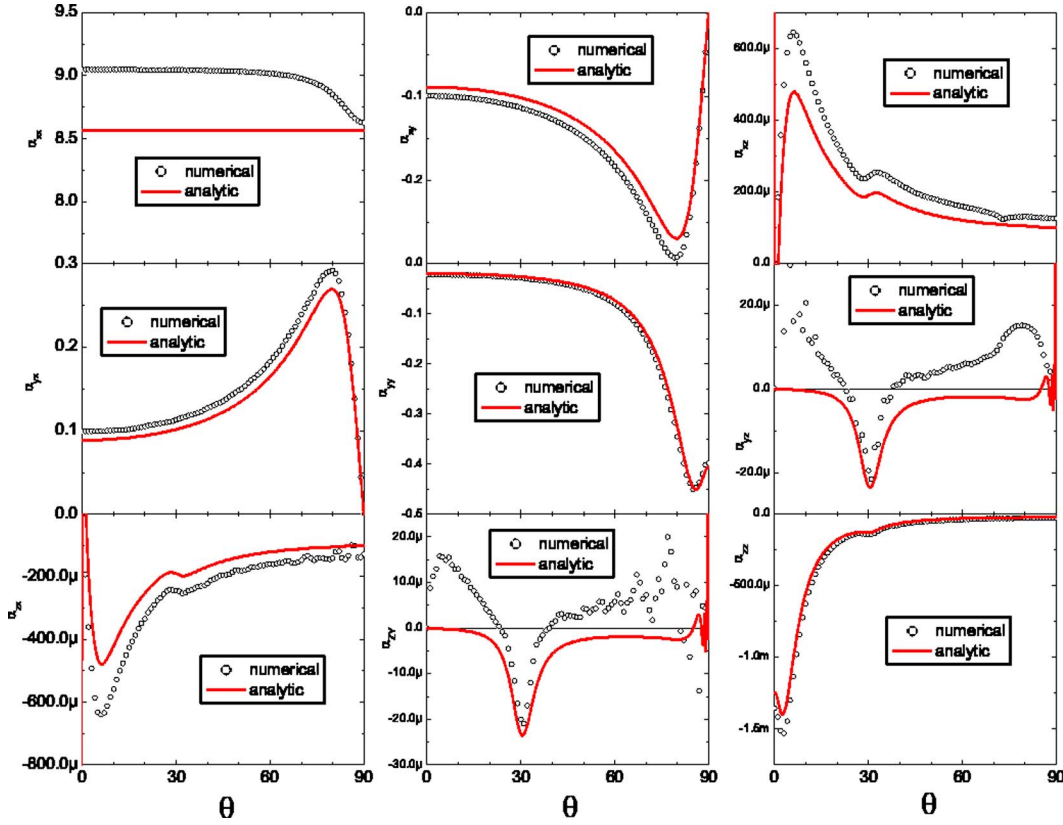$$v_y = \frac{2t_b b}{\hbar}\sin k_y b, \quad v_y = \frac{2t_c c}{\hbar}\sin k_z c. \quad (19)$$

FIG. 14. (Color online) Thermoelectric coefficient tensor $\overleftrightarrow{\alpha}$. In Boltzmann transport, $\overleftrightarrow{\alpha} \propto \partial\overleftrightarrow{\sigma}/\partial\varepsilon|_\mu$.

By substituting v_x in the equations of motion Eqs. (7), one can obtain analytic expressions for $k_y(t)$ and $k_z(t)$ and evaluate velocity averages $\langle \mathbf{v} \rangle$ for $\overleftrightarrow{\sigma}(\epsilon)$ by taking appropriate approximations. Then it is straightforward to obtain $\overleftrightarrow{\alpha}$ by differentiation. Details of the analytic calculation are presented in the Appendix. As shown in Figs. 12–15, our analytic calculations reproduce the main features of the numerical calculations. In some cases, the results from different methods overlap very well. Therefore, we believe our calculations describe the main behavior of the Nernst signal in Boltzmann transport within the tight binding approximation.

E. Results

Figure 12 shows the calculated angular dependence of the conductivity tensor $\overleftrightarrow{\sigma}$. The graphs are arranged in the pattern of the tensor elements σ_{ij} in the matrix form. Here θ is the magnetic field orientation respect to the c axis. Therefore $\theta = 90°$ corresponds to the magnetic field aligned with the b axis. As shown in the inset graph of σ_{zz}, there is a small hump at the first Lebed angle: $\mathbf{c}+\mathbf{b}$, which is about 30° in our approximation. This is one test that our calculations reproduce the angular dependence of σ_{zz} calculated by Osada *et al.*[40] By increasing the scattering time τ or the magnetic field strength, we can clearly resolve a peak at this angle. We also confirmed other AMROs, e.g., **ac** rotation and reproduce the Danner oscillations.[31] However, as far as we know, there is no calculation of the tensor $\overleftrightarrow{\alpha}$ in the literature for comparison. This was our motivation for performing the analytic

calculation to confirm our numerical results. Once we obtained $\overleftrightarrow{\sigma}$ and $\overleftrightarrow{\alpha}$, we got the thermoelectric power tensor $\overleftrightarrow{S}$ (Fig. 15) by taking the product of $\overleftrightarrow{\rho} = \overleftrightarrow{\sigma}^{-1}$ (Fig. 13) and $\overleftrightarrow{\alpha}$ (Fig. 14).

It is clear that the quality of the numerical calculation of $\overleftrightarrow{\sigma}$ is much better than that of $\overleftrightarrow{\alpha}$. Most curves of $\overleftrightarrow{\sigma}$ are very smooth and only minor oscillations are observed. Most curves of $\overleftrightarrow{\alpha}$ are smooth, except that α_{yz} and α_{zy}. α_{yz} has some spiky features for θ close to $\mathbf{c}$; while α_{zy} has some spiky features for θ close to $\mathbf{b}$. This is because the energy derivative of the velocities is very sensitive to the location on the Fermi surface (k_y, k_z). Finite size grid integration could also generate artificial spikes if the integrand oscillates a lot.

By varying the grid size and the integration cut-off limit, these artificial features can be suppressed, but at the expense of much more computation time. Since we are only interested in the general behaviors and magnitudes for a given set of parameters, we will use these nonperfect calculation results to compare with experiments, while keeping in mind that sharp features might be artificial. Also, our analytic results will help us to find most of the physical features.

The Nernst signal S_{zx} corresponds to the experimental results discussed in the previous section. It is clear that its angular dependence is similar to a $\sin \theta$ dependence, which agrees with the simple Drude model. The maximum magnitude is about 1 μV/K, which is two orders of magnitude smaller than what we found in our experiment as shown in Fig. 16. This result is very different in shape from our observation, missing the resonances at magic angles and it gives the wrong temperature dependence ($\overleftrightarrow{S} \propto T$ in Boltzmann
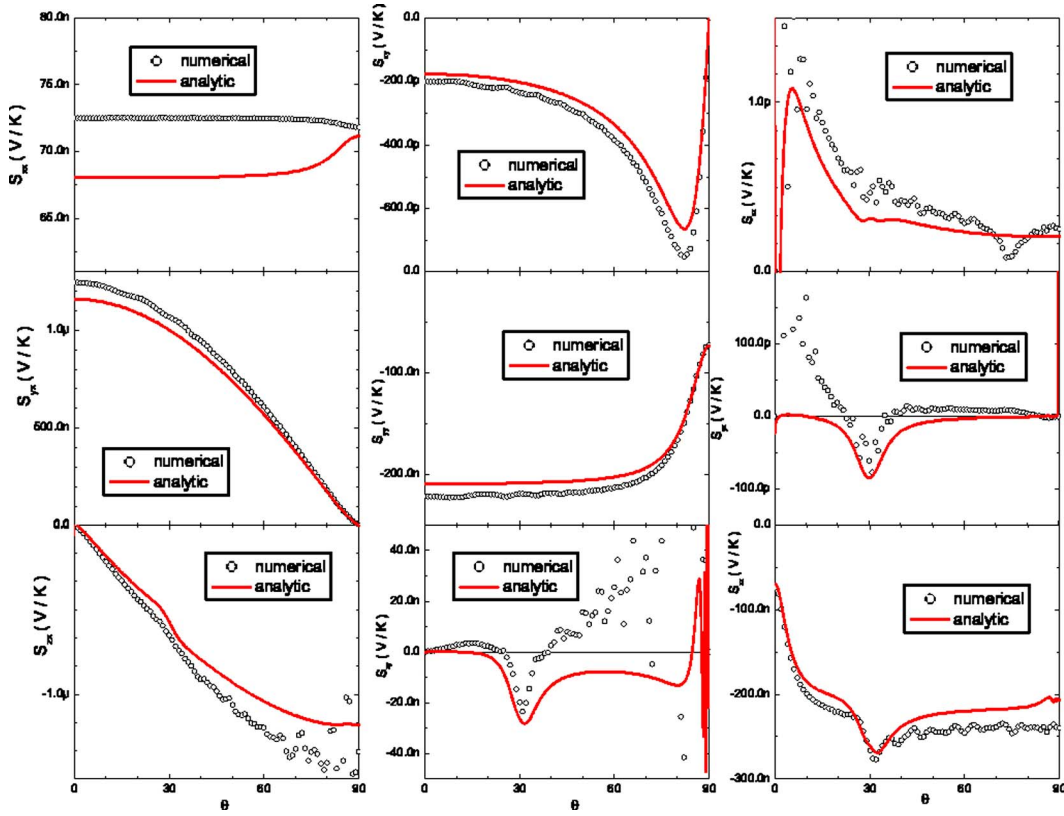
FIG. 15. (Color online) Thermoelectric power tensor $\overset{\leftrightarrow}{S}$, which is the product of resistivity tensor $\overset{\leftrightarrow}{\rho}$ (Fig. 13) and thermoelectric coefficient tensor $\overset{\leftrightarrow}{\alpha}$ (Fig. 14).

transport). Therefore, we conclude that the single particle picture is not able to describe the Nernst effect observed in $(TMTSF)_2PF_6$.

It is interesting to note that the Nernst signal S_{xz} has a similar angular dependence as the experimental Nernst effect S_{zx}, showing a peak near **c** and a sign change. However, the geometry is completely opposite and the value is about eight orders of magnitude too small. Experimentally we couldn't detect a sizable S_{xz}, though we did not optimize the experimental setup for that measurement.

Comparing the off-diagonal elements of $\overset{\leftrightarrow}{S}$ (i.e., the Nernst effect), we find that the elements in the upper triangle, S_{xy}, S_{xz}, and S_{yz} are much smaller that those in the lower triangle, S_{yx}, S_{zx}, and S_{zy}. More surprisingly, the conjugate elements don't have the same angular dependence. Does this violate the Onsager relation?[35,36] The answer is no. The Onsager relation only states constraints on σ and α and α' [defined in Eqs. (4)]:

$$\sigma_{ij}(H) = \sigma_{ji}(-H), \quad \alpha_{ij}(H) = \alpha'_{ji}(-H). \quad (20)$$

By symmetry, we know that $\sigma_{ij}(\alpha_{ij})$ is an odd function of magnetic field **H** for $i \neq j$.

$$\sigma_{ij}(H) = -\sigma_{ij}(-H), \quad \alpha_{ij}(H) = -\alpha_{ij}(-H). \quad (21)$$

Together with the Onsager relation Eq. (20), we can find

$$\sigma_{ij}(H) = -\sigma_{ji}(H), \quad \alpha_{ij}(H) = -\alpha_{ji}(H). \quad (22)$$

This is exactly what we see in the calculations [except $\sigma_{yz}(\alpha_{yz})$ and $\sigma_{zy}(\alpha_{zy})$, which are not real Hall effects since the magnetic field is in the plane]. However, the thermopower tensor $\overset{\leftrightarrow}{S}$ is the product of $\overset{\leftrightarrow}{\rho}$ and $\overset{\leftrightarrow}{\alpha}$. In general one should not expect $S_{ij} = -S_{ji}$. This is only true when we con-
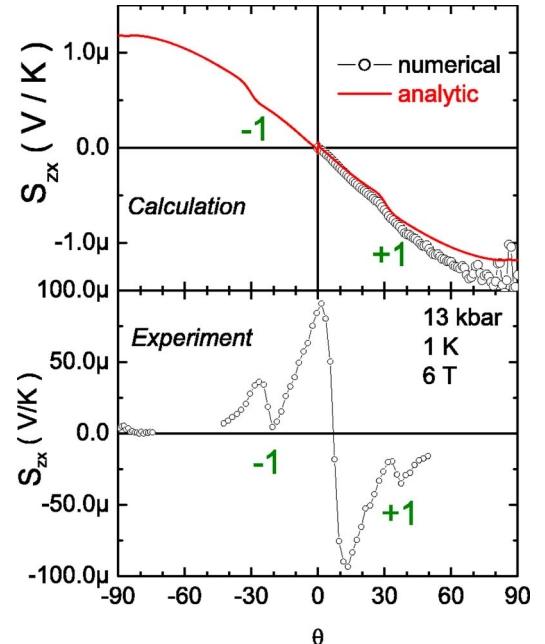

FIG. 16. (Color online) Comparison of S_{zx} between calculations (Fig. 15) and experimental data (Fig. 9).
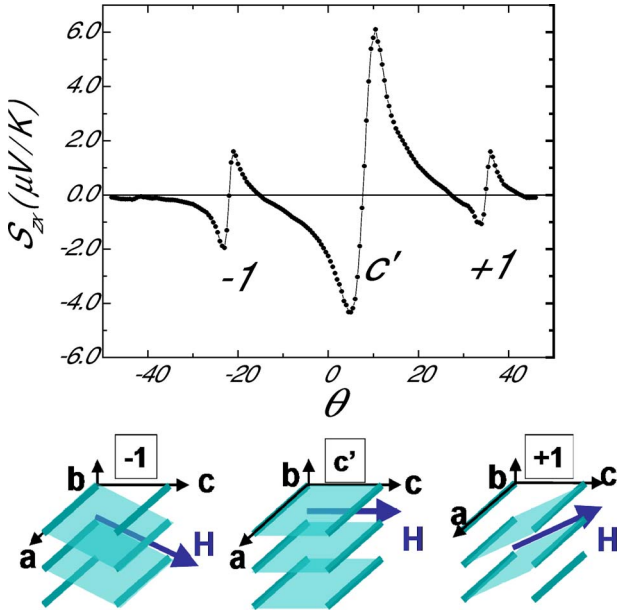
FIG. 17. (Color online) The schematic picture indicates that there is coherent transport only in the magic angle planes which are parallel to magnetic field. The Nernst signal would change sign as the field is rotated above or below these planes. $\boxed{-1}$: $\mathbf{B}\|-1\mathrm{L}$, $\mathbf{a}(\mathbf{c}'-\mathbf{b}')$ plane; $\boxed{\mathbf{c}'}$: $\mathbf{B}\|\mathbf{c}'$, $\mathbf{ac}'$ plane; $\boxed{+1}$: $\mathbf{B}\|+1\mathrm{L}$, $\mathbf{a}(\mathbf{c}'+\mathbf{b}')$ plane. The Nernst data are taken from previous measurements (Ref. 18).

FIG. 18. (Color online) Field induced interchain and/or interplane decoupling. $\boxed{1}$: $\mathbf{B}_\perp>\mathbf{B}^*$, $t_c^{\mathrm{eff}}=0$, chains are decoupled, Nernst signal is zero $S_{zx}=0$; $\boxed{2}$: $\mathbf{B}_\perp<\mathbf{B}^*$, $t_c^{\mathrm{eff}}\neq0$, chains are coupled, $S_{zx}>0$; $\boxed{3}$: $\mathbf{B}_\perp=0$, $t_c^{\mathrm{eff}}\neq0$, chains are coupled, $S_{zx}=0$; $\boxed{4}$: $\mathbf{B}_\perp<\mathbf{B}^*$, $t_c^{\mathrm{eff}}\neq0$, chains are coupled, $S_{zx}<0$; $\boxed{5}$: $\mathbf{B}_\perp>\mathbf{B}^*$, $t_c^{\mathrm{eff}}=0$, chains are decoupled, the Nernst signal is zero $S_{zx}=0$.

sider an isotropic system, where $\rho_{ii}=\rho_\circ$ and $\rho_{ij}=\rho_H$ for $i\neq j$. In an anisotropic system like (TMTSF)$_2$X, $\rho_{xx}\ll\rho_{yy}\ll\rho_{zz}$. If we ignore the Hall effect, we will have $S_{xy}\sim\rho_{xx}\alpha_{xy}\ll\rho_{yy}\alpha_{yx}\sim S_{yx}$. Nevertheless, the Nernst effect $S_{ij}(i\neq j)$ is an odd function of $\mathbf{H}$ and the Seebeck effect S_{ii} is an even function of $\mathbf{H}$ as long as there is a inversion symmetry.

In summary, we numerically and analytically calculated the thermopower tensor $\overleftrightarrow{S}$ by evaluating both the conductivity tensor $\overleftrightarrow{\sigma}$ and thermoelectric coefficient tensor $\overleftrightarrow{\alpha}$. The numerical results agree well with the analytic calculations. This gives us confidence on the reliability of our calculations. It is clear that Boltzmann transport within a single particle picture is not consistent with our observation in (TMTSF)$_2$PF$_6$. Therefore, correlation effects due to the strong e-e interaction should be considered in understanding the giant Nernst effect found in (TMTSF)$_2$PF$_6$. However, we note that the angular dependence of S_{zx} fits the data in (TMTSF)$_2$ClO$_4$ very well, though there is a factor of 10 or so difference in magnitude.[34] Our results are not limited to the Bechgaard salts (TMTSF)$_2$X. For any Q1D system with an open Fermi surface, all the transport coefficients can be calculated using our results based on Boltzmann transport in a tight binding model. Our original results should prove useful for further investigations.

IV. DISCUSSION

The giant value of the Nernst effect and the Nernst resonances at magic angles are not understood and it appears difficult to explain them in conventional Fermi liquid models as il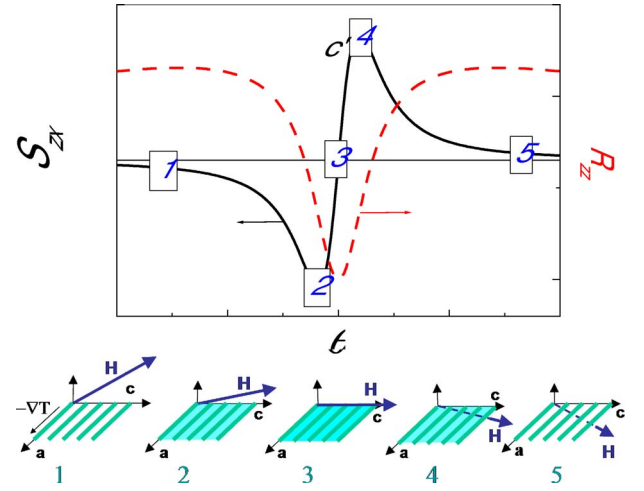lustrated by comparing our experiments with Boltzmann transport calculations. An exotic feature is that the Nernst signal changes its sign sharply at magic angles, with three "resonances" within 70° in our measurements. As we know, the sign of the transverse electric field is determined by the cross product: $\nabla T\times\mathbf{B}$. Of course, the physics really involves $\mathbf{E}=\mathbf{v}\times\mathbf{B}$. Since the temperature gradient is fixed, the only quantity that could possibly change its sign is the component of $\mathbf{B}$. As the magnetic field passes through a magic angle, the only component of magnetic field that could change sign relative to a magic angle is the one that is perpendicular to the direction of the magic angle. Therefore, we have to conclude that the Nernst signal in (TMTSF)$_2$PF$_6$ comes from $\mathbf{v}\times\mathbf{B}_\perp$. This means that whatever is moving is confined in the magic angle plane. The main idea that underlies our interpretation of the Nernst resonances is that the transport is only coherent at the planes which are "parallel" (or close to parallel) to the magnetic field. In other words, the coherent electronic motion is controlled by the orientation of the magnetic field relative to the planes defined by the conducting chains and the interchain directions (Fig. 17).

The nature of the coherence is not clear at this moment. One possibility is the quasiparticle coherence. For example we may have a field induced interchain and/or interplane decoupling picture. Figure 18 shows the basic idea of this picture. (TMTSF)$_2$PF$_6$ is a Q1D system, which consists of conduction chains along the a axis. The chains are weakly coupled with each other. When the magnetic field $\mathbf{B}$ is far from a magic angle, e.g, $\mathbf{c}'$, the interchain coherent coupling in this direction is effectively suppressed by the large normal field component, i.e., $t_c^{\mathrm{eff}}=0$ when $\mathbf{B}_\perp>\mathbf{B}^*$ (here $\mathbf{B}^*$ is a crossover magnetic field scale). In other words, there is no coherent transport in the $\mathbf{ac}$ plane for sufficient perpendicular field (Fig. 18$\boxed{1}$,$\boxed{5}$). When $\mathbf{B}$ is parallel to the $\mathbf{c}'$ direction, the coherent coupling in the $\mathbf{c}$ direction is restored and a coherent $\mathbf{ac}$ plane is formed (Fig. 18$\boxed{3}$). If we tilt the magnetic field slightly upward, there is a small component $\mathbf{B}_\perp$ of

B normal to this plane (Fig. 18[2]). Here $\delta\theta$ is small enough that $\mathbf{B}_\perp < \mathbf{B}^*$. So the plane is still coherent. In the presence of temperature gradient $-\nabla T$, there is a transverse electric field **B**, the Nernst effect. When we tilt the field slightly to the other side of the magic angle, everything is the same except the sign of $\mathbf{B}_\perp$ reverses. Therefore, the sign of the Nernst signal is reversed (Fig. 18[4]). This scenario is then repeated at the other magic angles as in Fig. 17.

In fact, the idea of field induced decoupling is not new. Strong et al.[10] considered the isolated conducting planes, **ab** planes, of $(TMTSF)_2PF_6$ as 2D non-Fermi-liquid due to the strong e-e interactions. The possible non-Fermi-liquid ground state of "isolated" $(TMTSF)_2PF_6$ chains is supported by transport,[41] optical,[24] and thermal transport[25] measurements. The effect of field induced coherent coupling (decoupling) is supported by temperature and angular dependence magnetoresistance studies.[42] However, this theory is not universally accepted due to the unknown nature of the non-Fermi-liquid state and the lack of a detailed model.

Another possibility is the 2D superconducting phase coherence proposed by Ong et al.[17] Ong points out that normal quasiparticles usually give a thermopower much larger than the Nernst signal,[20] whereas we have a large Nernst signal with undetectably small thermopower. On the contrary, vortex flow naturally produces an electric field that is predominantly transverse. This is generally true for most conventional systems, as well as HT_c cuprates.[20] Implicit in this model is the ability of the magnetic field to destroy phase coherence in the planes to which it is normal. It is natural that the vortices penetrating perpendicular planes destroy superconductivity. This is similar to the decoupling model discussed above and has the consequent "resonances" at magic angles.

V. CONCLUSION

We present a detailed study of the Nernst effect S_{zx} in $(TMTSF)_2PF_6$ as a function of temperature, pressure, magnetic field magnitude, and direction. The data agree well with our previous measurements.[18] We have calculated the Boltzmann transport coefficients by both numerical and analytic methods with realistic band parameters within the single relaxation time approximation. The two calculations agree with either very well, but fail to describe the experimental data. The large magnitude, resonantlike angular field dependence and the nonlinear field and temperature dependence cannot be understood within the semiclassical approximation of the Boltzmann transport. The sign change of the Nernst effect at magic angles strongly suggests that the transport is effectively 2D in lattice planes parallel or close to the orientation of magnetic field. The nature of the coherence is not clear at this moment. We suggest that the answer may lie in field induced decoupling of the strongly correlated chains.

ACKNOWLEDGMENT

APPENDIX

Here we describe the elements of our analytical treatment. We define $\phi_b \equiv k_y b$ and $\phi_c \equiv k_z c$. In the presence of a magnetic field in the **bc** plane, $\mathbf{B} = (0, B\sin\theta, B\cos\theta)$. Let us define $\omega_b^\theta \equiv \omega_b \cos\theta$ and $\omega_c^\theta \equiv \omega_c \sin\theta$. Here we have $\hbar\omega_b = |e|v_f Bb$ and $\hbar\omega_c = |e|v_f Bc$, $e < 0$ is the electron charge. Then the equations of motion become

$$\frac{d\phi_b}{dt} = \omega_b^\theta (1 - \beta\cos\phi_b - \gamma\cos\phi_c),$$

$$\frac{d\phi_c}{dt} = -\omega_c^\theta (1 - \beta\cos\phi_b - \gamma\cos\phi_c). \tag{A1}$$

The exact solutions are hard to obtain. However, since $\beta, \gamma \ll 1$, the solutions can be approximated to first order by an iterative method

$$\phi_b(t) \doteq \phi_b^0 + \omega_b^\theta t - \beta\sin(\phi_b^0 + \omega_b^\theta t) - \gamma\frac{\omega_b^\theta}{\omega_c^\theta}\sin(\phi_c^0 - \omega_c^\theta t),$$

$$\phi_c(t) \doteq \phi_c^0 - \omega_c^\theta t + \beta\frac{\omega_c^\theta}{\omega_b^\theta}\sin(\phi_b^0 + \omega_b^\theta t) - \gamma\sin(\phi_c^0 - \omega_c^\theta t). \tag{A2}$$

Note here $\omega_b^\theta/\omega_c^\theta$ diverges as $\theta \to 0$, and $\omega_c^\theta/\omega_b^\theta$ diverges as $\theta \to 90°$. So this solution is only good at $0 < \theta < 90°$. One has to be aware that as **B** approaches **b** or **c**, this solution may not give the correct result. With the help of Jacobi's expansions, it is straightforward to evaluate $\mathbf{v}(t)$ [Eq. (19)] and $\langle \mathbf{v} \rangle$. After tedious but straightforward calculation, we obtain the conductivity tensor $\overleftrightarrow{\sigma}$ [Eq. (A3)]. Here we use the approximation $\gamma \ll \beta \ll 1$, and only keep the leading terms in β, γ, β^2, and $\beta\gamma$. For simplicity, we also use the antisymmetric property of $\overleftrightarrow{\sigma}$

$$\sigma_{xx} = \frac{2e^2\tau}{\pi\hbar}\frac{v_f}{bc}[1 - \beta J_1(\beta) - \gamma J_1(\gamma)],$$

$$\sigma_{yx} = -\frac{2e^2\pi t_b}{\pi\hbar^2 c}\left\{\beta\frac{\omega_b^\theta\tau}{1+(\omega_b^\theta\tau)^2} - \frac{\beta^2}{2}J_1(\beta)\frac{2\omega_b^\theta\tau}{1+(2\omega_b^\theta\tau)^2}\right.$$
$$+ \left[\frac{\beta\gamma}{2}J_1\left(\gamma\frac{\omega_b^\theta}{\omega_c^\theta}\right) + \frac{\gamma^2}{2}J_1\left(\beta\frac{\omega_c^\theta}{\omega_b^\theta}\right)\right]$$
$$\left.\times\left[\frac{(\omega_b^\theta - \omega_c^\theta)\tau}{1+(\omega_b^\theta - \omega_c^\theta)^2\tau^2} - \frac{(\omega_b^\theta + \omega_c^\theta)\tau}{1+(\omega_b^\theta + \omega_c^\theta)^2\tau^2}\right]\right\}$$

and $\quad \sigma_{xy} = -\sigma_{yx},$

$$\sigma_{yy} = \frac{4e^2\pi t_b^2}{\pi\hbar^3 v_f}\frac{b}{c}\left\{\frac{1}{1+(\omega_b^\theta\tau)^2} + \frac{\beta J_1(\beta)}{2}\frac{1}{1+(2\omega_b^\theta\tau)^2}\right.$$
$$\left. + \frac{\gamma}{2}J_1\left(\gamma\frac{\omega_b^\theta}{\omega_c^\theta}\right)\left[\frac{1}{1+(\omega_b^\theta\tau - \omega_c^\theta\tau)^2} - \frac{1}{1+(\omega_b^\theta\tau + \omega_c^\theta\tau)^2}\right]\right\},$$

$$\sigma_{zx} = \frac{2e^2\pi t_c}{\pi b\hbar^2}\left\{\gamma\frac{\omega_c^\theta\tau}{1+(\omega_c^\theta\tau)^2} + \frac{\gamma^2}{2}J_1(\gamma)\frac{2\omega_c^\theta\tau}{1+(2\omega_c^\theta\tau)^2}\right.$$

$$-\left[\frac{\beta^2}{2}J_1\left(\gamma\frac{\omega_b^\theta}{\omega_c^\theta}\right) + \frac{\beta\gamma}{2}J_1\left(\beta\frac{\omega_c^\theta}{\omega_b^\theta}\right)\right]$$

$$\left.\times\left[\frac{(\omega_b^\theta-\omega_c^\theta)\tau}{1+(\omega_b^\theta-\omega_c^\theta)^2\tau^2} + \frac{(\omega_b^\theta+\omega_c^\theta)\tau}{1+(\omega_b^\theta+\omega_c^\theta)^2\tau^2}\right]\right\}$$

and $\sigma_{xz} = -\sigma_{zx}$,

$$\sigma_{yz} = \frac{2e^2\pi t_b t_c}{\pi\hbar^3 v_f}\gamma J_1\left(\beta\frac{\omega_c^\theta}{\omega_b^\theta}\right)\left[\frac{1}{1+(\omega_b^\theta\tau+\omega_c^\theta\tau)^2}\right.$$

$$\left.+\frac{1}{1+(\omega_b^\theta\tau-\omega_c^\theta\tau)^2}\right],$$

$$\sigma_{zy} = \frac{2e^2\pi t_b t_c}{\pi\hbar^3 v_f}\beta J_1\left(\gamma\frac{\omega_b^\theta}{\omega_c^\theta}\right)\left[\frac{1}{1+(\omega_b^\theta\tau-\omega_c^\theta\tau)^2}\right.$$

$$\left.+\frac{1}{1+(\omega_b^\theta\tau+\omega_c^\theta\tau)^2}\right],$$

$$\sigma_{zz} = \frac{4e^2\pi t_c^2 c}{\pi\hbar^3 v_f b}\left\{\frac{1}{1+(\omega_c^\theta\tau)^2} - \frac{\gamma J_1(\gamma)}{2}\frac{1}{1+(2\omega_c^\theta\tau)^2}\right.$$

$$\left.+\frac{\beta}{2}J_1\left(\beta\frac{\omega_c^\theta}{\omega_b^\theta}\right)\left[\frac{1}{1+(\omega_b^\theta\tau-\omega_c^\theta\tau)^2} - \frac{1}{1+(\omega_b^\theta\tau+\omega_c^\theta\tau)^2}\right]\right\}.$$

$$(A3)$$

It is clear from Fig. 12 that the analytic calculation reproduces the numerical results very well. Due to the limitation of our expansion, not every minor detail was reproduced. For example, in this first order approximation, σ_{xx} is independent of the angle in analytic form, while numerically it shows a very weak angle dependence. The good agreement between different calculations give us confidence about the reliability of the calculations. Once we know the analytic form of the conductivity tensor $\overleftrightarrow{\sigma}$, we can take its energy derivative to obtain $\overleftrightarrow{\alpha}$ [Eq. (A4)]. From Eq. (1) we can obtain the thermoelectric power tensor $\overleftrightarrow{S}$. The analytic form of $\overleftrightarrow{S}$ would be too long to write down here since every term in $\overleftrightarrow{S}$ is the sum of three products of two matrix elements. We just numerically calculate the matrix product. Here we only present the angular dependence of all quantities in order to compare with the experiment. In principle one could obtain temperature and field dependence with these formula

$$\alpha_{xx} = -\frac{2\pi k_B^2 Te\tau a}{3\hbar^2 bc}\{(1 - \beta J_1(\beta) - \gamma J_1(\gamma))$$

$$+3[\beta J_1(\beta) + \beta^2 J_1'(\beta) + \gamma J_1(\gamma) + \gamma^2 J_1'(\gamma)]\},$$

$$\alpha_{yx} = \frac{4\pi k_B^2 Te\tau}{3\hbar^2 c}\frac{t_b^2}{t_a^2}\frac{\omega_b^\theta\tau[1+2(\omega_b^\theta\tau)^2]}{[1+(\omega_b^\theta\tau)^2]^2},$$

$$\alpha_{xy} = -\alpha_{yx},$$

$$\alpha_{zx} = \frac{2\pi k_B^2 Te\tau}{3\hbar^2 b}\left\{\gamma^2\frac{\omega_c^\theta\tau[1+2(\omega_c^\theta\tau)^2]}{[1+(\omega_c^\theta\tau)^2]^2}\right.$$

$$-\frac{\gamma^3}{4}\frac{2\omega_c^\theta\tau}{1+(2\omega_c^\theta\tau)^2}\left[J_1(\gamma)\frac{5+7(2\omega_c^\theta\tau)^2}{1+(2\omega_c^\theta\tau)^2} + 3\gamma J_1'(\gamma)\right]$$

$$-\frac{\gamma\beta}{2}\left[\beta J_1\left(\gamma\frac{\omega_b^\theta}{\omega_c^\theta}\right) + \gamma J_1\left(\beta\frac{\omega_c^\theta}{\omega_b^\theta}\right)\right]$$

$$\times\left[\frac{(\omega_b^\theta\tau-\omega_c^\theta\tau)[5+7(\omega_b^\theta\tau-\omega_c^\theta\tau)^2]}{[1+(\omega_b^\theta\tau-\omega_c^\theta\tau)^2]^2}\right.$$

$$\left.+\frac{(\omega_b^\theta\tau+\omega_c^\theta\tau)[5+7(\omega_b^\theta\tau+\omega_c^\theta\tau)^2]}{[1+(\omega_b^\theta\tau+\omega_c^\theta\tau)^2]^2}\right]$$

$$-\frac{3\gamma\beta}{4}\left[\beta\gamma\frac{\omega_b^\theta}{\omega_c^\theta}J_1'\left(\gamma\frac{\omega_b^\theta}{\omega_c^\theta}\right) + \gamma\beta\frac{\omega_c^\theta}{\omega_b^\theta}J_1'\left(\beta\frac{\omega_c^\theta}{\omega_b^\theta}\right)\right]$$

$$\left.\times\left[\frac{\omega_b^\theta\tau-\omega_c^\theta\tau}{1+(\omega_b^\theta\tau-\omega_c^\theta\tau)^2} + \frac{\omega_b^\theta\tau+\omega_c^\theta\tau}{1+(\omega_b^\theta\tau+\omega_c^\theta\tau)^2}\right]\right\},$$

$$\alpha_{xz} = -\alpha_{zx},$$

$$\alpha_{yy} = \frac{2\pi k_B^2 Te\tau b}{3\hbar^2 ac}\frac{t_b^2}{t_a^2}\frac{1+3(\omega_b^\theta\tau)^2}{[1+(\omega_b^\theta\tau)^2]^2},$$

$$\alpha_{yz} = \frac{\pi k_B^2 Te\tau\beta\gamma^2}{3\hbar^2 a}\left\{J_1\left(\beta\frac{\omega_c^\theta}{\omega_b^\theta}\right)\left[\frac{2+3(\omega_b^\theta\tau-\omega_c^\theta\tau)^2}{[1+(\omega_b^\theta\tau-\omega_c^\theta\tau)^2]^2}\right.\right.$$

$$\left.+\frac{2+3(\omega_b^\theta\tau+\omega_c^\theta\tau)^2}{[1+(\omega_b^\theta\tau+\omega_c^\theta\tau)^2]^2}\right] + \frac{3\beta\omega_c^\theta}{2\omega_b^\theta}J_1'\left(\beta\frac{\omega_c^\theta}{\omega_b^\theta}\right)$$

$$\left.\times\left[\frac{1}{1+(\omega_b^\theta\tau-\omega_c^\theta\tau)^2} + \frac{1}{1+(\omega_b^\theta\tau+\omega_c^\theta\tau)^2}\right]\right\},$$

$$\alpha_{zy} = \frac{\pi k_B^2 Te\tau\gamma\beta^2}{3\hbar^2 a}\left\{J_1\left(\gamma\frac{\omega_b^\theta}{\omega_c^\theta}\right)\left[\frac{2+3(\omega_b^\theta\tau-\omega_c^\theta\tau)^2}{[1+(\omega_b^\theta\tau-\omega_c^\theta\tau)^2]^2}\right.\right.$$

$$\left.+\frac{2+3(\omega_b^\theta\tau+\omega_c^\theta\tau)^2}{[1+(\omega_b^\theta\tau+\omega_c^\theta\tau)^2]^2}\right] + \frac{3\gamma\omega_b^\theta}{2\omega_c^\theta}J_1'\left(\gamma\frac{\omega_b^\theta}{\omega_c^\theta}\right)$$

$$\left.\times\left[\frac{1}{1+(\omega_b^\theta\tau-\omega_c^\theta\tau)^2} + \frac{1}{1+(\omega_b^\theta\tau+\omega_c^\theta\tau)^2}\right]\right\},$$

$$\alpha_{zz} = \frac{\pi k_B^2 Te\tau\gamma^2 c}{\hbar^2 ab}\left\{\frac{1+3(\omega_c^\theta\tau)^2}{[1+(\omega_c^\theta\tau)^2]^2} - \frac{\gamma J_1(\gamma)}{2}\frac{7+11\cdot(2\omega_c^\theta\tau)^2}{[1+(2\omega_c^\theta\tau)^2]^2}\right.$$

$$-\frac{3\gamma^2 J_1'(\gamma)}{1+(2\omega_c^\theta\tau)^2} + \beta J_1\left(\beta\frac{\omega_c^\theta}{\omega_b^\theta}\right)\left[\frac{2+3(\omega_b^\theta\tau-\omega_c^\theta\tau)^2}{[1+(\omega_b^\theta\tau-\omega_c^\theta\tau)^2]^2}\right.$$

$$\left.-\frac{2+3(\omega_b^\theta\tau+\omega_c^\theta\tau)^2}{[1+(\omega_b^\theta\tau+\omega_c^\theta\tau)^2]^2}\right] + 3\beta\frac{\omega_c^\theta}{\omega_b^\theta}J_1'\left(\beta\frac{\omega_c^\theta}{\omega_b^\theta}\right)$$

$$\left.\times\left[\frac{1}{1+(\omega_b^\theta\tau-\omega_c^\theta\tau)^2} - \frac{1}{1+(\omega_b^\theta\tau+\omega_c^\theta\tau)^2}\right]\right\}. \quad (A4)$$

*Present address: Department of Physics, University of Texas, Austin, Texas 78712.

[1] I. J. Lee, M. J. Naughton, G. M. Danner, and P. M. Chaikin, Phys. Rev. Lett. **78**, 3555 (1997).

[2] I. J. Lee, S. E. Brown, W. G. Clark, M. J. Strouse, M. J. Naughton, W. Kang, and P. M. Chaikin, Phys. Rev. Lett. **88**, 017004 (2002).

[3] I. J. Lee, P. M. Chaikin, and M. J. Naughton, Phys. Rev. Lett. **88**, 207002 (2002).

[4] T. Ishiguro, K. Yamaji, and G. Saito, *Organic Superconductor* (Springer, New York, 1997).

[5] T. Osada, A. Kawasumi, S. Kagoshima, N. Miura, and G. Saito, Phys. Rev. Lett. **66**, 1525 (1991).

[6] M. J. Naughton, O. H. Chung, M. Chaparala, X. Bu, and P. Coppens, Phys. Rev. Lett. **67**, 3712 (1991).

[7] W. Kang, S. T. Hannahs, and P. M. Chaikin, Phys. Rev. Lett. **69**, 2827 (1992).

[8] A. G. Lebed, Sov. Phys. JETP **43**, 137 (1986).

[9] A. G. Lebed and P. Bak, Phys. Rev. Lett. **63**, 1315 (1989).

[10] S. P. Strong, D. G. Clarke, and P. W. Anderson, Phys. Rev. Lett. **73**, 1007 (1994).

[11] T. Osada, S. Kagoshima, and N. Miura, Phys. Rev. B **46**, 1812 (1992).

[12] T. Osada, Physica B **256**, 633 (1998).

[13] K. Maki, Phys. Rev. B **45**, R5111 (1992).

[14] V. M. Yakovenko, Phys. Rev. Lett. **68**, 3607 (1992).

[15] P. M. Chaikin, Phys. Rev. Lett. **69**, 2831 (1992).

[16] A. G. Lebed, J. Phys. I **6**, 1819 (1996).

[17] N. P. Ong, W. Wu, P. M. Chaikin, and P. W. Anderson, Europhys. Lett. **66**, 579 (2004).

[18] W. Wu, I. J. Lee, and P. M. Chaikin, Phys. Rev. Lett. **91**, 056601 (2003).

[19] E. S. Choi, J. S. Brooks, H. Kang, Y. J. Jo, and W. Kang, Phys. Rev. Lett. **95**, 187001 (2005).

[20] Y. Wang, Z. A. Xu, T. Kakeshita, S. Uchida, S. Ono, Y. Ando, and N. P. Ong, Phys. Rev. B **64**, 224519 (2001).

[21] Y. Wang, N. P. Ong, Z. A. Xu, T. Kakeshita, S. Uchida, D. A. Bonn, R. Liang, and W. N. Hardy, Phys. Rev. Lett. **88**, 257003 (2002).

[22] Y. Wang, S. Ono, Y. Onose, G. Gu, Y. Ando, Y. Tokura, S. Uchida, and N. P. Ong, Science **299**, 86 (2002).

[23] W. Wu, P. M. Chaikin, W. Kang, J. Shinagawa, W. Yu, and S. E. Brown, Phys. Rev. Lett. **94**, 097004 (2005).

[24] V. Vescoli, L. Degiorgi, W. Henderson, G. Grner, K. P. Starkey, and L. K. Montgomery, Science **281**, 1181 (1998).

[25] T. Lorenz, M. Hofmann, M. Gruninger, A. Freimuth, G. S. Uhrig, M. Dumm, and M. Dressel, Nature (London) **418**, 614 (2002).

[26] R. Yu, Ph.D. thesis, University of Pennsylvania, 1990.

[27] W. Wu, Ph.D. thesis, Princeton University, 2004.

[28] B. D. Josephson, Phys. Lett. **1**, 251 (1962).

[29] B. D. Josephson, Adv. Phys. **14**, 419 (1965).

[30] W. Kang, S. T. Hannahs, and P. M. Chaikin, Phys. Rev. Lett. **70**, 3091 (1993).

[31] G. M. Danner, W. Kang, and P. M. Chaikin, Phys. Rev. Lett. **72**, 3714 (1994).

[32] T. Osada, S. Kagoshima, and N. Miura, Phys. Rev. Lett. **77**, 5261 (1996).

[33] I. J. Lee and M. J. Naughton, Phys. Rev. B **57**, 7423 (1998).

[34] M.-S. Nam, A. Ardavan, W. Wu, and P. M. Chaikin (unpublished).

[35] L. Onsager, Phys. Rev. **37**, 405 (1931).

[36] L. Onsager, Phys. Rev. **38**, 2265 (1931).

[37] N. W. Ashcroft and N. D. Mermin, *Solid State Physics* (Saunders, Philadelphia, 1976).

[38] W. H. Press, B. P. Flannery, S. A. Teukolsky, and W. T. Vetterling, *Numerical Recipes in Pascal: The Art of Scientific Computing* (Cambridge University Press, Cambridge, 1991).

[39] A. G. Lebed, N. N. Bagmet, and M. J. Naughton, Phys. Rev. Lett. **93**, 157006 (2004).

[40] T. Osada, N. Kami, R. Kondo, and S. Kagoshima, Synth. Met. **103**, 2024 (1999).

[41] G. M. Danner and P. M. Chaikin, Phys. Rev. Lett. **75**, 4690 (1995).

[42] E. I. Chasheshikina, Ph.D. thesis, Princeton University, 1998.